

Einstein@Home search for periodic gravitational waves in early S5 LIGO data

B. P. Abbott,¹⁷ R. Abbott,¹⁷ R. Adhikari,¹⁷ P. Ajith,² B. Allen,^{2,61} G. Allen,³⁵ R. S. Amin,²¹ S. B. Anderson,¹⁷ W. G. Anderson,⁶¹ M. A. Arain,⁴⁸ M. Araya,¹⁷ H. Armandula,¹⁷ P. Armor,⁶¹ Y. Aso,¹⁷ S. Aston,⁴⁶ P. Aufmuth,¹⁶ C. Aulbert,² S. Babak,¹ P. Baker,²⁴ S. Ballmer,¹⁷ C. Barker,¹⁸ D. Barker,¹⁸ B. Barr,⁴⁹ P. Barriga,⁶⁰ L. Barsotti,²⁰ M. A. Barton,¹⁷ I. Bartos,¹⁰ R. Bassiri,⁴⁹ M. Bastarrika,⁴⁹ B. Behnke,¹ M. Benacquista,⁴² J. Betzwieser,¹⁷ P. T. Beyersdorf,³¹ I. A. Bilenko,²⁵ G. Billingsley,¹⁷ R. Biswas,⁶¹ E. Black,¹⁷ J. K. Blackburn,¹⁷ L. Blackburn,²⁰ D. Blair,⁶⁰ B. Bland,¹⁸ T. P. Bodiya,²⁰ L. Bogue,¹⁹ R. Bork,¹⁷ V. Boschi,¹⁷ S. Bose,⁶² P. R. Brady,⁶¹ V. B. Braginsky,²⁵ J. E. Brau,⁵⁴ D. O. Bridges,¹⁹ M. Brinkmann,² A. F. Brooks,¹⁷ D. A. Brown,³⁶ A. Brummit,³⁰ G. Brunet,²⁰ A. Bullington,³⁵ A. Buonanno,⁵⁰ O. Burmeister,² R. L. Byer,³⁵ L. Cadonati,⁵¹ J. B. Camp,²⁶ J. Cannizzo,²⁶ K. C. Cannon,¹⁷ J. Cao,²⁰ L. Cardenas,¹⁷ S. Caride,⁵² G. Castaldi,⁵⁷ S. Caudill,²¹ M. Cavaglia,³⁹ C. Cepeda,¹⁷ T. Chalermongsak,¹⁷ E. Chalkley,⁴⁹ P. Charlton,⁹ S. Chatterji,¹⁷ S. Chelkowski,⁴⁶ Y. Chen,^{1,6} N. Christensen,⁸ C. T. Y. Chung,³⁸ D. Clark,³⁵ J. Clark,⁷ J. H. Clayton,⁶¹ T. Cokelaer,⁷ C. N. Colacino,¹² R. Conte,⁵⁶ D. Cook,¹⁸ T. R. C. Corbitt,²⁰ N. Cornish,²⁴ D. Coward,⁶⁰ D. C. Coyne,¹⁷ J. D. E. Creighton,⁶¹ T. D. Creighton,⁴² A. M. Cruise,⁴⁶ R. M. Culter,⁴⁶ A. Cumming,⁴⁹ L. Cunningham,⁴⁹ S. L. Danilishin,²⁵ K. Danzmann,^{2,16} B. Daudert,¹⁷ G. Davies,⁷ E. J. Daw,⁴⁰ D. DeBra,³⁵ J. Degallaix,² V. Dergachev,⁵² S. Desai,³⁷ R. DeSalvo,¹⁷ S. Dhurandhar,¹⁵ M. Díaz,⁴² A. Dietz,⁷ F. Donovan,²⁰ K. L. Dooley,⁴⁸ E. E. Doomes,³⁴ R. W. P. Drever,⁵ J. Dueck,² I. Duke,²⁰ J. -C. Dumas,⁶⁰ J. G. Dwyer,¹⁰ C. Echols,¹⁷ M. Edgar,⁴⁹ A. Effler,¹⁸ P. Ehrens,¹⁷ G. Ely,⁸ E. Espinoza,¹⁷ T. Etzel,¹⁷ M. Evans,²⁰ T. Evans,¹⁹ S. Fairhurst,⁷ Y. Faltas,⁴⁸ Y. Fan,⁶⁰ D. Fazi,¹⁷ H. Fehrmann,² L. S. Finn,³⁷ K. Flasch,⁶¹ S. Foley,²⁰ C. Forrest,⁵⁵ N. Fotopoulos,⁶¹ A. Franzen,¹⁶ M. Frede,² M. Frei,⁴¹ Z. Frei,¹² A. Freise,⁴⁶ R. Frey,⁵⁴ T. Fricke,¹⁹ P. Fritschel,²⁰ V. V. Frolov,¹⁹ M. Fyffe,¹⁹ V. Galdi,⁵⁷ J. A. Garofoli,³⁶ I. Gholami,¹ J. A. Giaime,^{21,19} S. Giampanis,² K. D. Giardino,¹⁹ K. Goda,²⁰ E. Goetz,⁵² L. M. Goggin,⁶¹ G. González,²¹ M. L. Gorodetsky,²⁵ S. Gößler,² R. Gouaty,²¹ A. Grant,⁴⁹ S. Gras,⁶⁰ C. Gray,¹⁸ M. Gray,⁴ R. J. S. Greenhalgh,³⁰ A. M. Gretarsson,¹¹ F. Grimaldi,²⁰ R. Grosso,⁴² H. Grote,² S. Grunewald,¹ M. Guenther,¹⁸ E. K. Gustafson,¹⁷ R. Gustafson,⁵² B. Hage,¹⁶ J. M. Hallam,⁴⁶ D. Hammer,⁶¹ G. D. Hammond,⁴⁹ C. Hanna,¹⁷ J. Hanson,¹⁹ J. Harms,⁵³ G. M. Harry,²⁰ I. W. Harry,⁷ E. D. Harstad,⁵⁴ K. Haughian,⁴⁹ K. Hayama,⁴² J. Heefner,¹⁷ I. S. Heng,⁴⁹ A. Heptonstall,¹⁷ M. Hewitson,² S. Hild,⁴⁶ E. Hirose,³⁶ D. Hoak,¹⁹ K. A. Hodge,¹⁷ K. Holt,¹⁹ D. J. Hosken,⁴⁵ J. Hough,⁴⁹ D. Hoyland,⁶⁰ B. Hughey,²⁰ S. H. Huttner,⁴⁹ D. R. Ingram,¹⁸ T. Isogai,⁸ M. Ito,⁵⁴ A. Ivanov,¹⁷ B. Johnson,¹⁸ W. W. Johnson,²¹ D. I. Jones,⁵⁸ G. Jones,⁷ R. Jones,⁴⁹ L. Ju,⁶⁰ P. Kalmus,¹⁷ V. Kalogera,²⁸ S. Kandhasamy,⁵³ J. Kanner,⁵⁰ D. Kasprzyk,⁴⁶ E. Katsavounidis,²⁰ K. Kawabe,¹⁸ S. Kawamura,²⁷ F. Kawazoe,² W. Kells,¹⁷ D. G. Keppel,¹⁷ A. Khalaidovski,² F. Y. Khalili,²⁵ R. Khan,¹⁰ E. Khazanov,¹⁴ P. King,¹⁷ J. S. Kissel,²¹ S. Klimenko,⁴⁸ K. Kokeyama,²⁷ V. Kondrashov,¹⁷ R. Kopparapu,³⁷ S. Koranda,⁶¹ D. Kozak,¹⁷ B. Krishnan,¹ R. Kumar,⁴⁹ P. Kwee,¹⁶ P. K. Lam,⁴ M. Landry,¹⁸ B. Lantz,³⁵ A. Lazzarini,¹⁷ H. Lei,⁴² M. Lei,¹⁷ N. Leindecker,³⁵ I. Leonor,⁵⁴ C. Li,⁶ H. Lin,⁴⁸ P. E. Lindquist,¹⁷ T. B. Littenberg,²⁴ N. A. Lockerbie,⁵⁹ D. Lodhia,⁴⁶ M. Longo,⁵⁷ M. Lormand,¹⁹ P. Lu,³⁵ M. Lubinski,¹⁸ A. Lucianetti,⁴⁸ H. Lück,^{2,16} B. Machenschalk,¹ M. MacInnis,²⁰ M. Mageswaran,¹⁷ K. Mailand,¹⁷ I. Mandel,²⁸ V. Mandic,⁵³ S. Márka,¹⁰ Z. Márka,¹⁰ A. Markosyan,³⁵ J. Markowitz,²⁰ E. Maros,¹⁷ I. W. Martin,⁴⁹ R. M. Martin,⁴⁸ J. N. Marx,¹⁷ K. Mason,²⁰ F. Matichard,²¹ L. Matone,¹⁰ R. A. Matzner,⁴¹ N. Mavalvala,²⁰ R. McCarthy,¹⁸ D. E. McClelland,⁴ S. C. McGuire,³⁴ M. McHugh,²³ G. McIntyre,¹⁷ D. J. A. McKechnan,⁷ K. McKenzie,⁴ M. Mehmet,² A. Melatos,³⁸ A. C. Melissinos,⁵⁵ D. F. Menéndez,³⁷ G. Mendell,¹⁸ R. A. Mercer,⁶¹ S. Meshkov,¹⁷ C. Messenger,² M. S. Meyer,¹⁹ J. Miller,⁴⁹ J. Minelli,³⁷ Y. Mino,⁶ V. P. Mitrofanov,²⁵ G. Mitselmakher,⁴⁸ R. Mittleman,²⁰ O. Miyakawa,¹⁷ B. Moe,⁶¹ S. D. Mohanty,⁴² S. R. P. Mohapatra,⁵¹ G. Moreno,¹⁸ T. Morioka,²⁷ K. Mors,² K. Mossavi,² C. MowLowry,⁴ G. Mueller,⁴⁸ H. Müller-Ebhardt,² D. Muhammad,¹⁹ S. Mukherjee,⁴² H. Mukhopadhyay,¹⁵ A. Mullavey,⁴ J. Munch,⁴⁵ P. G. Murray,⁴⁹ E. Myers,¹⁸ J. Myers,¹⁸ T. Nash,¹⁷ J. Nelson,⁴⁹ G. Newton,⁴⁹ A. Nishizawa,²⁷ K. Numata,²⁶ J. O'Dell,³⁰ B. O'Reilly,¹⁹ R. O'Shaughnessy,³⁷ E. Ochsner,⁵⁰ G. H. Ogin,¹⁷ D. J. Ottaway,⁴⁵ R. S. Ottens,⁴⁸ H. Overmier,¹⁹ B. J. Owen,³⁷ Y. Pan,⁵⁰ C. Pankow,⁴⁸ M. A. Papa,^{1,61} V. Parameshwaraiah,¹⁸ P. Patel,¹⁷ M. Pedraza,¹⁷ S. Penn,¹³ A. Perraca,⁴⁶ V. Pierro,⁵⁷ I. M. Pinto,⁵⁷ M. Pitkin,⁴⁹ H. J. Pletsch,² M. V. Plissi,⁴⁹ F. Postiglione,⁵⁶ M. Principe,⁵⁷ R. Prix,² L. Prokhorov,²⁵ O. Punken,² V. Quetschke,⁴⁸ F. J. Raab,¹⁸ D. S. Rabeling,⁴ H. Radkins,¹⁸ P. Raffai,¹² Z. Raics,¹⁰ N. Rainer,² M. Rakhmanov,⁴² V. Raymond,²⁸ C. M. Reed,¹⁸ T. Reed,²² H. Rehbein,² S. Reid,⁴⁹ D. H. Reitze,⁴⁸ R. Riesen,¹⁹ K. Riles,⁵² B. Rivera,¹⁸ P. Roberts,³ N. A. Robertson,^{17,49} C. Robinson,⁷ E. L. Robinson,¹ S. Roddy,¹⁹ C. Röver,² J. Rollins,¹⁰ J. D. Romano,⁴² J. H. Romie,¹⁹ S. Rowan,⁴⁹ A. Rüdiger,² P. Russell,¹⁷ K. Ryan,¹⁸ S. Sakata,²⁷ L. Sancho de la Jordana,⁴⁴ V. Sandberg,¹⁸ V. Sannibale,¹⁷ L. Santamaría,¹ S. Saraf,³² P. Sarin,²⁰ B. S. Sathyaprakash,⁷ S. Sato,²⁷ M. Satterthwaite,⁴ P. R. Saulson,³⁶

R. Savage,¹⁸ P. Savov,⁶ M. Scanlan,²² R. Schilling,² R. Schnabel,² R. Schofield,⁵⁴ B. Schulz,² B. F. Schutz,^{1,7} P. Schwinberg,¹⁸ J. Scott,⁴⁹ S. M. Scott,⁴ A. C. Searle,¹⁷ B. Sears,¹⁷ F. Seifert,² D. Sellers,¹⁹ A. S. Sengupta,¹⁷ A. Sergeev,¹⁴ B. Shapiro,²⁰ P. Shawhan,⁵⁰ D. H. Shoemaker,²⁰ A. Sibley,¹⁹ X. Siemens,⁶¹ D. Sigg,¹⁸ S. Sinha,³⁵ A. M. Sintes,⁴⁴ B. J. J. Slagmolen,⁴ J. Slutsky,²¹ J. R. Smith,³⁶ M. R. Smith,¹⁷ N. D. Smith,²⁰ K. Somiya,⁶ B. Sorazu,⁴⁹ A. Stein,²⁰ L. C. Stein,²⁰ S. Steplewski,⁶² A. Stochino,¹⁷ R. Stone,⁴² K. A. Strain,⁴⁹ S. Strigin,²⁵ A. Stroeer,²⁶ A. L. Stuver,¹⁹ T. Z. Summerscales,³ K. -X. Sun,³⁵ M. Sung,²¹ P. J. Sutton,⁷ G. P. Szokoly,¹² D. Talukder,⁶² L. Tang,⁴² D. B. Tanner,⁴⁸ S. P. Tarabrin,²⁵ J. R. Taylor,² R. Taylor,¹⁷ J. Thacker,¹⁹ K. A. Thorne,¹⁹ K. S. Thorne,⁶ A. Thüring,¹⁶ K. V. Tokmakov,⁴⁹ C. Torres,¹⁹ C. Torrie,¹⁷ G. Traylor,¹⁹ M. Trias,⁴⁴ D. Ugolini,⁴³ J. Ulmen,³⁵ K. Urbanek,³⁵ H. Vahlbruch,¹⁶ M. Vallisneri,⁶ C. Van Den Broeck,⁷ M. V. van der Sluys,²⁸ A. A. van Veggel,⁴⁹ S. Vass,¹⁷ R. Vaulin,⁶¹ A. Vecchio,⁴⁶ J. Veitch,⁴⁶ P. Veitch,⁴⁵ C. Veltkamp,² A. Villar,¹⁷ C. Vorvick,¹⁸ S. P. Vyachanin,²⁵ S. J. Waldman,²⁰ L. Wallace,¹⁷ R. L. Ward,¹⁷ A. Weidner,² M. Weinert,² A. J. Weinstein,¹⁷ R. Weiss,²⁰ L. Wen,^{6,60} S. Wen,²¹ K. Wette,⁴ J. T. Whelan,^{1,29} S. E. Whitcomb,¹⁷ B. F. Whiting,⁴⁸ C. Wilkinson,¹⁸ P. A. Willems,¹⁷ H. R. Williams,³⁷ L. Williams,⁴⁸ B. Willke,^{2,16} I. Wilmot,³⁰ L. Winkelmann,² W. Winkler,² C. C. Wipf,²⁰ A. G. Wiseman,⁶¹ G. Woan,⁴⁹ R. Wooley,¹⁹ J. Worden,¹⁸ W. Wu,⁴⁸ I. Yakushin,¹⁹ H. Yamamoto,¹⁷ Z. Yan,⁶⁰ S. Yoshida,³³ M. Zanolin,¹¹ J. Zhang,⁵² L. Zhang,¹⁷ C. Zhao,⁶⁰ N. Zotov,²² M. E. Zucker,²⁰ H. zur Mühlen,¹⁶ and J. Zweizig¹⁷

(The LIGO Scientific Collaboration, <http://www.ligo.org>)

D. P. Anderson⁴⁷

¹Albert-Einstein-Institut, Max-Planck-Institut für Gravitationsphysik, D-14476 Golm, Germany

²Albert-Einstein-Institut, Max-Planck-Institut für Gravitationsphysik, D-30167 Hannover, Germany

³Andrews University, Berrien Springs, MI 49104 USA

⁴Australian National University, Canberra, 0200, Australia

⁵California Institute of Technology, Pasadena, CA 91125, USA

⁶Caltech-CaRT, Pasadena, CA 91125, USA

⁷Cardiff University, Cardiff, CF24 3AA, United Kingdom

⁸Carleton College, Northfield, MN 55057, USA

⁹Charles Sturt University, Wagga Wagga, NSW 2678, Australia

¹⁰Columbia University, New York, NY 10027, USA

¹¹Embry-Riddle Aeronautical University, Prescott, AZ 86301 USA

¹²Eötvös University, ELTE 1053 Budapest, Hungary

¹³Hobart and William Smith Colleges, Geneva, NY 14456, USA

¹⁴Institute of Applied Physics, Nizhny Novgorod, 603950, Russia

¹⁵Inter-University Centre for Astronomy and Astrophysics, Pune - 411007, India

¹⁶Leibniz Universität Hannover, D-30167 Hannover, Germany

¹⁷LIGO - California Institute of Technology, Pasadena, CA 91125, USA

¹⁸LIGO - Hanford Observatory, Richland, WA 99352, USA

¹⁹LIGO - Livingston Observatory, Livingston, LA 70754, USA

²⁰LIGO - Massachusetts Institute of Technology, Cambridge, MA 02139, USA

²¹Louisiana State University, Baton Rouge, LA 70803, USA

²²Louisiana Tech University, Ruston, LA 71272, USA

²³Loyola University, New Orleans, LA 70118, USA

²⁴Montana State University, Bozeman, MT 59717, USA

²⁵Moscow State University, Moscow, 119992, Russia

²⁶NASA/Goddard Space Flight Center, Greenbelt, MD 20771, USA

²⁷National Astronomical Observatory of Japan, Tokyo 181-8588, Japan

²⁸Northwestern University, Evanston, IL 60208, USA

²⁹Rochester Institute of Technology, Rochester, NY 14623, USA

³⁰Rutherford Appleton Laboratory, HSIC, Chilton, Didcot, Oxon OX11 0QX United Kingdom

³¹San Jose State University, San Jose, CA 95192, USA

³²Sonoma State University, Rohnert Park, CA 94928, USA

³³Southeastern Louisiana University, Hammond, LA 70402, USA

³⁴Southern University and A&M College, Baton Rouge, LA 70813, USA

³⁵Stanford University, Stanford, CA 94305, USA

³⁶Syracuse University, Syracuse, NY 13244, USA

³⁷The Pennsylvania State University, University Park, PA 16802, USA

³⁸The University of Melbourne, Parkville VIC 3010, Australia

³⁹The University of Mississippi, University, MS 38677, USA

⁴⁰The University of Sheffield, Sheffield S10 2TN, United Kingdom

⁴¹The University of Texas at Austin, Austin, TX 78712, USA

⁴²The University of Texas at Brownsville and Texas Southmost College, Brownsville, TX 78520, USA

⁴³Trinity University, San Antonio, TX 78212, USA

⁴⁴Universitat de les Illes Balears, E-07122 Palma de Mallorca, Spain

⁴⁵University of Adelaide, Adelaide, SA 5005, Australia

⁴⁶University of Birmingham, Birmingham, B15 2TT, United Kingdom

⁴⁷University of California at Berkeley, Berkeley, CA 94720 USA

⁴⁸University of Florida, Gainesville, FL 32611, USA

⁴⁹University of Glasgow, Glasgow, G12 8QQ, United Kingdom

⁵⁰University of Maryland, College Park, MD 20742 USA

⁵¹University of Massachusetts - Amherst, Amherst, MA 01003, USA

⁵²University of Michigan, Ann Arbor, MI 48109, USA

⁵³University of Minnesota, Minneapolis, MN 55455, USA

⁵⁴University of Oregon, Eugene, OR 97403, USA

⁵⁵University of Rochester, Rochester, NY 14627, USA

⁵⁶University of Salerno, 84084 Fisciano (Salerno), Italy

⁵⁷University of Sannio at Benevento, I-82100 Benevento, Italy

⁵⁸University of Southampton, Southampton, SO17 1BJ, United Kingdom

⁵⁹University of Strathclyde, Glasgow, G1 1XQ, United Kingdom

⁶⁰University of Western Australia, Crawley, WA 6009, Australia

⁶¹University of Wisconsin-Milwaukee, Milwaukee, WI 53201, USA

⁶²Washington State University, Pullman, WA 99164, USA

(Dated: October 28, 2018)

This paper reports on an all-sky search for periodic gravitational waves from sources such as deformed isolated rapidly-spinning neutron stars. The analysis uses 840 hours of data from 66 days of the fifth LIGO science run (S5). The data was searched for quasi-monochromatic waves with frequencies f in the range from 50 Hz to 1500 Hz, with a linear frequency drift \dot{f} (measured at the solar system barycenter) in the range $-f/\tau < \dot{f} < 0.1 f/\tau$, for a minimum spin-down age τ of 1 000 years for signals below 400 Hz and 8 000 years above 400 Hz. The main computational work of the search was distributed over approximately 100 000 computers volunteered by the general public. This large computing power allowed the use of a relatively long coherent integration time of 30 hours while searching a large parameter space. This search extends Einstein@Home's previous search in LIGO S4 data to about three times better sensitivity. No statistically significant signals were found. In the 125 Hz to 225 Hz band, more than 90% of sources with dimensionless gravitational-wave strain tensor amplitude greater than 3×10^{-24} would have been detected.

PACS numbers: 04.80.Nn, 95.55.Ym, 97.60.Gb, 07.05.Kf

I. INTRODUCTION

Gravitational waves (GW) are predicted by Einstein's general theory of relativity, but have so far eluded direct detection. The Laser Interferometer Gravitational-wave Observatory (LIGO) [1, 2] has been built for this purpose and is currently the most sensitive gravitational-wave detector in operation.

Rapidly rotating neutron stars are expected to generate periodic gravitational-wave signals through various mechanisms [3, 4, 5, 6, 7, 8, 9]. Irrespective of the emission mechanism, these signals are quasi-monochromatic with a slowly changing intrinsic frequency. Additionally, at a terrestrial detector, such as LIGO, the data analysis problem is complicated by the fact that the periodic GW signals are Doppler modulated by the detector's motion relative to the solar system barycenter (SSB).

A previous paper [10] reported on the results of the Einstein@Home search for periodic GW signals in the data from LIGO's fourth science run (S4). The present work extends this search, using more sensitive data from 66 days of LIGO's fifth science run (S5).

Because of the weakness of the GW signals buried in

the detector noise, the data analysis strategy is critical. A powerful detection method is given by coherent matched-filtering. This means one convolves all available data with a set of template waveforms corresponding to all possible putative sources. The resulting detection statistic is derived in Ref. [11] and is commonly referred to as the \mathcal{F} -statistic.

The parameter space to be scanned for putative signals from isolated neutron stars is four-dimensional, with two parameters required to describe the source sky position using standard astronomical equatorial coordinates α (right ascension) and δ (declination), and additional coordinates (f, \dot{f}) denoting the intrinsic frequency and frequency drift. To achieve the maximum possible sensitivity, the template waveforms must match the source waveforms to within a fraction of a cycle over the entire observation time (months or years for current data samples). So one must choose a very closely spaced grid of templates in this four-dimensional parameter space. This makes the computational cost of the search very high, and therefore limits the search sensitivity [12].

To maximize the possible integration time, and hence achieve a more sensitive search, the computation was

distributed via the volunteer computing project Einstein@Home [13]. This large computing power allowed the use of a relatively long coherent integration time of 30 h, despite the large parameter space searched. Thus, this search involves coherent matched-filtering in the form of the \mathcal{F} -statistic over 30-hour-long data segments and subsequent incoherent combination of \mathcal{F} -statistic results via a coincidence strategy.

The methods used here are further described in Sections II-IV. Estimates of the sensitivity of this search and results are in Sections V and VI, respectively. Previously, other all-sky searches for periodic GW sources using LIGO S4 and S5 data, which combine power from many short coherent segments (30-minute intervals) of data, have been reported by the LIGO Scientific Collaboration (LSC) [14, 15]. However, this Einstein@Home search explores large regions of parameter space which have not been analyzed previously with LIGO S5 data. The sensitivity of the results here are compared with previous searches in Section VII, and conclusions are given in Section VIII.

II. DATA SELECTION AND PREPARATION

The data analyzed in the present work was collected between November 19, 2005 and January 24, 2006. The total data set covering frequencies from 50 Hz to 1500 Hz consisted of 660 h of data from the LIGO Hanford 4-km (H1) detector and 180 h of data from the LIGO Livingston 4-km (L1) detector.

The data preparation method is essentially identical to that of the previous S4 analysis [10]. Therefore only a brief summary of the main aspects is given here; further details are found in [10] and references therein. The data set has been divided into segments of 30 h each. However, the 30-hour long data segments are not contiguous, but have time gaps. Since the number of templates required increases rapidly with observation span, the 30 h of data for each segment were chosen to lie within a time span of less than 40 h. In what follows, the notion of “segment” will always refer to one of these time stretches, each of which contains exactly $T = 30$ h of data. The total time spanned by a given data segment j is denoted by $T_{\text{span},j}$ and conforms to $30 \text{ h} < T_{\text{span},j} < 40 \text{ h}$.

Given the above constraints, a total of $N_{\text{seg}} = 28$ data segments (22 from H1, 6 from L1) were obtained from the early S5 data considered. These data segments are labeled by $j = 1, \dots, 28$. Table I lists the global positioning system (GPS) start time along with the time span of each segment.

In this analysis, the maximum frequency shift of a signal over the length of any given data segment and parameter-space range examined is dominated by the Doppler modulation due to the Earth’s orbital motion around the solar system barycenter (SSB), while the effects of frequency change resulting from intrinsic spin-down of the source are smaller. The orbital velocity of

TABLE I: Segments of early S5 data used in this search. The columns are the data segment index j , the GPS start time t_j and the time spanned $T_{\text{span},j}$.

j	Detector	t_j [s]	$T_{\text{span},j}$ [s]
1	H1	816397490	140768
2	H1	816778879	134673
3	H1	816993218	134697
4	H1	817127915	137962
5	H1	817768509	142787
6	H1	817945327	143919
7	H1	818099543	139065
8	H1	818270501	143089
9	H1	818552200	134771
10	H1	818721347	138570
11	H1	818864047	134946
12	H1	819337064	143091
13	H1	819486815	120881
14	H1	819607696	116289
15	H1	819758149	136042
16	H1	820482173	143904
17	H1	820628379	138987
18	H1	821214511	126307
19	H1	821340818	126498
20	H1	821630884	141913
21	H1	821835537	138167
22	H1	821973704	142510
23	L1	818812286	130319
24	L1	819253562	140214
25	L1	819393776	126075
26	L1	819547883	138334
27	L1	820015400	121609
28	L1	821291797	140758

the Earth is about $v/c \approx 10^{-4}$, hence a signal will always remain in a narrow frequency band smaller than ± 0.15 Hz around a given source frequency. Therefore, for each detector the total frequency range from 50 Hz to 1500 Hz is broken up into 2900 slices, each of 0.5 Hz bandwidth plus overlapping wings of 0.175 Hz on either side.

The detector data contains numerous narrow-band noise artifacts, so-called “lines”, which are of instrumental origin, such as harmonics of the 60 Hz mains frequency. Prior to the analysis, line features of understood origin (at the time before the launch of the search) were removed (“cleaned”) from the data by substitution of the frequency-domain data bins with random Gaussian noise. Table III in the Appendix shows the frequencies of lines excluded from the data. The harmonic mean noise strain amplitude spectra of the final cleaned H1 and L1 data sets are shown in Fig. 1.

III. DATA PROCESSING

The paper describing the previous Einstein@Home search in S4 data [10] presented in detail the data processing scheme. For the purpose of the present search the

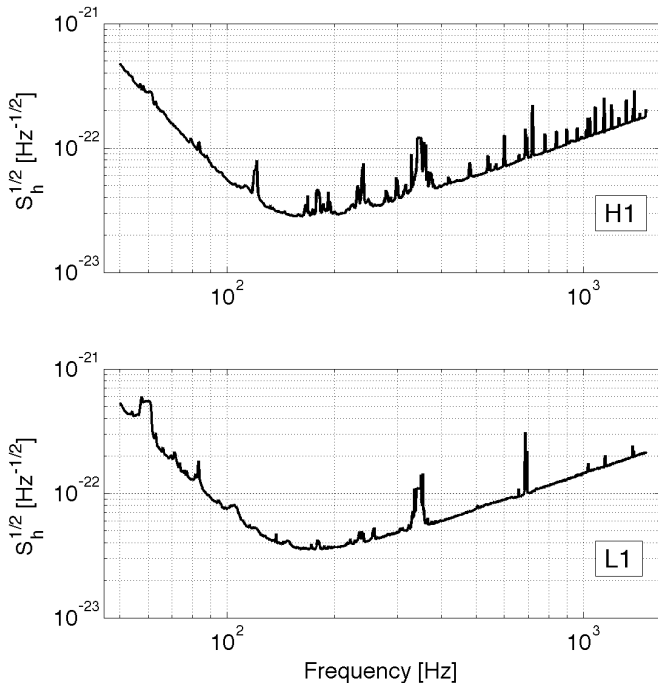


FIG. 1: Strain amplitude spectral densities $\sqrt{S_h(f)}$ of the cleaned data from the LIGO detectors H1 (top) and L1 (bottom) used in the Einstein@Home searches. The curves in the top (bottom) panel are the harmonic mean of the 22 H1 (6 L1) 30-hour segments of S5 data used this Einstein@Home analysis.

same data processing infrastructure is employed. Hence, here only a short summary thereof is given, pointing out the minimal changes applied in setting up the present analysis.

The total computation of the search is broken up into 16 446 454 workunits. Each workunit represents a separate computing task and is processed using the Berkeley Open Infrastructure for Network Computing (BOINC) [16, 17, 18]. To eliminate errors and weed out results that are wrong, each workunit is independently processed by at least two different volunteers. Once two successful results for a workunit are returned back to the Einstein@Home server, they are compared by an automatic validator, which discards results that differ by more than some allowed tolerance. New workunits are generated and run independently again for such cases.

In searching for periodic gravitational-wave signals, each workunit examines a different part of parameter space. A key design goal is that the computational effort to conduct the entire analysis should take about 6–7 months. An additional design goal is to minimize the download burden on the Einstein@Home volunteers’ internet connections and also on the Einstein@Home data servers. This is accomplished by letting each workunit use only a small re-usable subset of the total data set, so that Einstein@Home volunteers are able to carry out useful computations on a one-day time scale.

Each workunit searches only one data segment over a

narrow frequency range, but covering all of the sky and the entire range of frequency derivatives. The workunits are labeled by three indices (j, k, ℓ) , where $j = 1, \dots, 28$ denotes the data segment, $k = 1, \dots, 2900$ labels the 0.5 Hz frequency band and $\ell = 1, \dots, M(j, k)$ enumerates the individual workunits pertinent to data segment j and frequency band k .

In each segment the \mathcal{F} -statistic is evaluated on a grid in parameter space. Each parameter-space grid is constructed such that grid points (templates) are not further apart from their nearest neighbor by more than a certain distance. The distance measure is defined from a metric on parameter space, first introduced in [19, 20], representing the fractional loss of squared signal-to-noise ratio (SNR^2) due to waveform mismatch between the putative signal and the template. For any given workunit, the parameter-space grid is a Cartesian product of uniformly-spaced steps df in frequency, uniformly-spaced steps $d\dot{f}$ in frequency derivative, and a two-dimensional sky grid, which has non-uniform spacings determined by the metric [10, 21].

For frequencies in the range [50, 400) Hz, the maximal allowed mismatch was chosen as $m = 0.15$ (corresponding to a maximal loss in SNR^2 of 15%), while in the range [400, 1500) Hz, the maximal mismatch was $m = 0.4$. It can be shown [10, 21], that these choices of maximal mismatch enable a coherent search of near-optimal sensitivity at fixed computational resources.

The step-size in frequency f obtained from the metric depends on $T_{\text{span},j}$ of the j ’th data segment: $df_j = 2\sqrt{3m}/(\pi T_{\text{span},j})$. In the low-frequency range this results in frequency spacings in the range $df_j \in [2.97, 3.67] \mu\text{Hz}$, while for high-frequency workunits $df_j \in [4.85, 6.0] \mu\text{Hz}$.

The range of frequency derivatives \dot{f} searched is defined in terms of the “spin-down age” $\tau \equiv -f/\dot{f}$, namely $\tau \geq 1000$ years for low-frequency and $\tau \geq 8000$ years for high-frequency workunits. As in the S4 Einstein@Home search, these ranges were guided by the assumption that a nearby very young neutron star would correspond to a historical supernova, supernova remnant, known pulsar, or pulsar wind nebula. The search also covers a small “spin-up” range, so the actual ranges searched are $\dot{f} \in [-f/\tau, 0.1f/\tau]$. In \dot{f} the grid points are spaced according to $d\dot{f}_j = 12\sqrt{5m}/(\pi T_{\text{span},j}^2)$, resulting in resolutions $d\dot{f}_j \in [1.60, 2.44] \times 10^{-10} \text{ Hz/s}$ for low-frequency workunits, and $d\dot{f}_j \in [2.61, 3.99] \times 10^{-10} \text{ Hz/s}$ for high-frequency workunits.

The resolution of the search grid in the sky depends both on the start time t_j and duration $T_{\text{span},j}$ of the segment, as well as on the frequency f . The number of grid points on the sky scales as $\propto f^2$, and approximately as $\propto T_{\text{span},j}^{2.4}$ for the range of $T_{\text{span},j} \sim 30 - 40$ h used in this search. As was done in the previous S4 analysis [10], to simplify the construction of workunits and limit the number of different input files to be sent, the sky grids are fixed over a frequency range of 10 Hz, but differ for

each data segment j . The sky grids are computed at the higher end of each 10-Hz band, so they are slightly “over-covering” the sky at lower frequencies within the band. The search covers in total a frequency band of 1450 Hz, so there are 145 different sky grids for each segment.

The output from one workunit in the low (high) frequency range contains the top 1000 (10000) candidate events with the largest values of the \mathcal{F} -statistic. In order to balance the load on the Einstein@Home servers, a low-frequency workunit returns a factor of 10 fewer events, because low-frequency workunits require runtimes approximately 10 times shorter than high-frequency workunits. For each candidate event five values are reported: frequency (Hz), right ascension angle (radians), declination angle (radians), frequency derivative (Hz/s) and $2\mathcal{F}$ (dimensionless). The frequency is the frequency at the SSB at the instant of the first data point in the corresponding data segment. Returning only the “loudest” candidate events effectively corresponds to a floating threshold on the value of the \mathcal{F} -statistic. This avoids large lists of candidate events being produced in regions of parameter space containing non-Gaussian noise, such as instrumental artifacts that were not removed *a priori* from the input data because of unknown origin.

IV. POST-PROCESSING

After results for each workunit are returned to the Einstein@Home servers by project volunteers, post-processing is conducted on those servers and on dedicated computing clusters. The post-processing has the goal of finding candidate events that appear in many of the 28 different data segments with consistent parameters.

In this search, the post-processing methods are the same as used for the Einstein@Home S4 search [10]. Therefore, this section only summarizes the main steps; a more detailed description can be found in [10].

A consistent (coincident) set of “candidate events” is called a “candidate”. Candidate events from different data segments are considered coincident if they cluster closely together in the four-dimensional parameter space. By using a grid of “coincidence cells”, the clustering method can reliably detect strong signals, which would produce candidate events with closely-matched parameters in many of the 28 data segments. The post-processing pipeline operates in 0.5 Hz-wide frequency bands, and performs the following steps described below.

A. The post-processing steps

A putative source with non-zero spin-down would generate candidate events with different apparent frequency values in each data segment. To account for these effects, the frequencies of the candidate events are shifted back to the same frequency value at fiducial time t_{fiducial} via $f(t_{\text{fiducial}}) = f(t_j) + (t_{\text{fiducial}} - t_j)\dot{f}$, where \dot{f} and $f(t_j)$

are the spin-down rate and frequency of a candidate event reported by the search code in the result file, and t_j is the time-stamp of the first datum in the j 'th data segment. The fiducial time is chosen to be the GPS start time of the earliest ($j = 1$) data segment, $t_{\text{fiducial}} = t_1 = 816\,397\,490$ s.

A grid of cells is then constructed in the four-dimensional parameter space to find coincidences among the 28 different data segments. The coincidence search algorithm uses rectangular cells in the coordinates $(f, \dot{f}, \alpha \cos \delta, \delta)$. The dimensions of the cells are adapted to the parameter-space search grid (see below). Each candidate event is assigned to a particular cell. In cases where two or more candidate events from the same data segment j fall into the same cell, only the candidate event having the largest value of $2\mathcal{F}$ is retained in the cell. Then the number of candidate events per cell coming from distinct data segments is counted, to identify cells with more coincidences than would be expected by random chance.

To ensure that candidate events located on opposite sides of a cell border are not missed, the entire cell coincidence grid is shifted by half a cell width in all possible $2^4 = 16$ combinations of the four parameter-space dimensions. Hence, 16 different coincidence cell grids are used in the analysis.

B. Construction of coincidence windows

The coincidence cells are constructed to be as small as possible to reduce the probability of false alarms. However, since each of the 28 different data segments uses a different parameter space grid, the coincidence cells must be chosen to be large enough that the candidate events from a source (which would appear at slightly different points in parameter space in each of the 28 data segments) would still lie in the same coincidence cell.

In the frequency direction, the size Δf for the coincidence cell is given by the largest search grid spacing in f (for smallest value of $T_{\text{span},j}$) plus the largest possible offset in spin-down: $\Delta f = \max_j (df_j + \Delta t df_j)$, where the maximization over j selects the data segment with the smallest $T_{\text{span},j}$ (which is $j = 6$) and $\Delta t = |\max_j t_j - \min_j t_j| = t_{22} - t_1 = 5\,576\,214$ s is the total time span between the latest and earliest data segments. For safety, e.g. against noise fluctuations that could shift a candidate peak, Δf has been increased by a further 30%, so that the width of the coincidence cell in f below 400 Hz is $\Delta f = 1.78$ mHz and $\Delta f = 2.9$ mHz above 400 Hz.

In the frequency-derivative direction, the size of the coincidence cell is given by the largest df_j spacing in the parameter space grid, which is also determined by the smallest value of $T_{\text{span},j}$. For safety this is also increased by 30%, so that $\Delta \dot{f} = 3.18 \times 10^{-10}$ Hz s⁻¹ below 400 Hz and $\Delta \dot{f} = 5.19 \times 10^{-10}$ Hz s⁻¹ above 400 Hz.

In sky position, the size of the coincidence cells

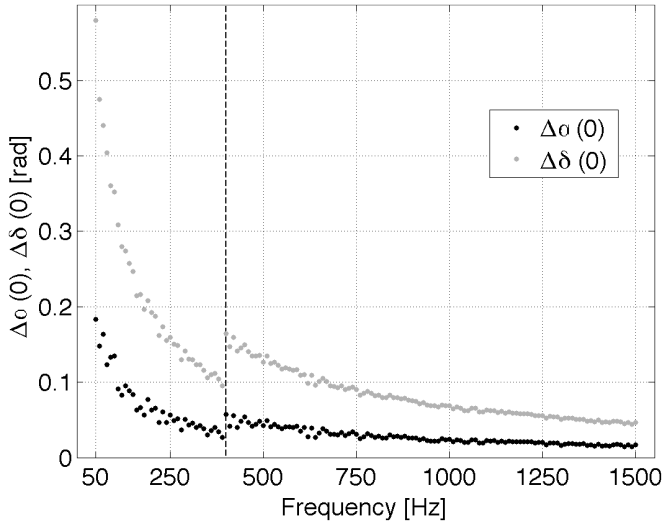


FIG. 2: The parameters $\Delta\alpha(0)$ and $\Delta\delta(0)$ of the sky coincidence-window model as a function of the 10 Hz frequency band. The vertical dashed line at 400 Hz indicates the separation between the low and high frequency ranges.

is guided by the behavior of the parameter-space metric. As described in [10], the density of grid points in the sky is approximately proportional to $|\cos(\delta)\sin(\delta)| \propto |\sin(2\delta)|$, and it follows from [10] that $\cos(\delta)d\alpha = |\sin(\delta)|d\delta = \text{const}$. Because of the singularity when $\delta \rightarrow 0$, a useful model for the coincidence window size varying with declination is given by

$$\begin{aligned} \Delta\alpha(\delta) &= \Delta\alpha(0)/\cos(\delta) \\ \Delta\delta(\delta) &= \begin{cases} \Delta\delta(0) & \text{if } |\delta| < \delta_c, \\ \Delta\alpha(0)/|\sin(|\delta| - \kappa\Delta\alpha(0))| & \text{if } |\delta| \geq \delta_c. \end{cases} \end{aligned} \quad (1)$$

To ensure continuity at $\delta = \delta_c$, the transition point δ_c is defined by the condition $\Delta\alpha(0)/|\sin(|\delta_c| - \kappa\Delta\alpha(0))| = \Delta\delta(0)$. The tuning parameter κ is chosen based on visual inspection to be $\kappa = 1.5$ in this search. The values of $\Delta\alpha(0)$ and $\Delta\delta(0)$ are directly determined from the sky grids (see [10] for details). Figure 2 shows these parameters for all sky grids as a function of frequency. As stated above, the sky grids are constant for 10 Hz-wide steps in frequency, and so these parameters vary with the same step-size.

C. Output of the post-processing

The output of the post-processing is a list of the candidates with the greatest number of coincidences. The possible number of coincidences ranges from a minimum of 0 to a maximum of 28 (the number of data segments analyzed). The meaning of \mathcal{C} coincidences is that there are \mathcal{C} candidate events within a given coincidence cell. In each frequency band of coincidence-window width Δf , the coincidence cell containing the largest number of candidate events is found. The pipeline outputs the average

frequency of the coincidence cell, the average sky position and spin-down of the candidate events, the number of candidate events in the coincidence cell, and the “significance” of the candidate. The significance of a candidate, first introduced in [22] and explained in [10], is defined by

$$\mathcal{S} = \sum_{q=1}^{\mathcal{C}} (\mathcal{F}_q - \ln(1 + \mathcal{F}_q)), \quad (2)$$

where \mathcal{F}_q is the \mathcal{F} -statistic value of the q ’th candidate event in the same coincidence cell, which harbors a total of \mathcal{C} candidate events.

D. False alarm probability and detection threshold

The central goal of this search is to make a *confident detection*, not to set upper limits with the broadest possible coverage band. This is reflected in the choice of detection threshold based on the expected false alarm rates. In this search the background level of false alarm candidates is expected at 10 coincidences (out of 28 possible). As a pragmatic choice, the threshold of confident detection is set at 20 coincidences, which is highly improbable to arise from random noise only. These settings will be elucidated in the following.

To calculate the false alarm probabilities, consider the case where $\mathcal{E}_{\text{seg}}(k)$ candidate events per data segment obtained from pure Gaussian noise are distributed uniformly about $N_{\text{cell}}(k)$ independent coincidence cells in a given 0.5 Hz band k . Assuming the candidate events are independent, the probability $p_{\text{F}}(k; \mathcal{C}_{\text{max}})$ per coincidence cell of finding \mathcal{C}_{max} or more candidate events from different data segments has been derived in [10] and is given by the binomial distribution

$$p_{\text{F}}(k; \mathcal{C}_{\text{max}}) = \sum_{n=\mathcal{C}_{\text{max}}}^{N_{\text{seg}}} \binom{N_{\text{seg}}}{n} [\epsilon(k)]^n [1 - \epsilon(k)]^{N_{\text{seg}} - n}, \quad (3)$$

where $\epsilon(k)$ denotes the probability of populating any given coincidence cell with one or more candidate events in a given data segment, obtained as

$$\epsilon(k) = 1 - \left(1 - \frac{1}{N_{\text{cell}}(k)}\right)^{\mathcal{E}_{\text{seg}}(k)}. \quad (4)$$

Finally, the probability $P_{\text{F}}(k; \mathcal{C}_{\text{max}})$ that there are \mathcal{C}_{max} or more coincidences in *one or more* of the N_{cell} cells per 0.5 Hz band k is

$$P_{\text{F}}(k; \mathcal{C}_{\text{max}}) = 1 - [1 - p_{\text{F}}(k; \mathcal{C}_{\text{max}})]^{N_{\text{cell}}}. \quad (5)$$

Figure 3 shows the dependence of $P_{\text{F}}(k; \mathcal{C}_{\text{max}})$ on the frequency bands for different values of \mathcal{C}_{max} . One finds that the average false alarm probability of obtaining 10 or more coincidences is approximately 10^{-3} . This means, in our analysis of 2900 half-Hz frequency bands, only a

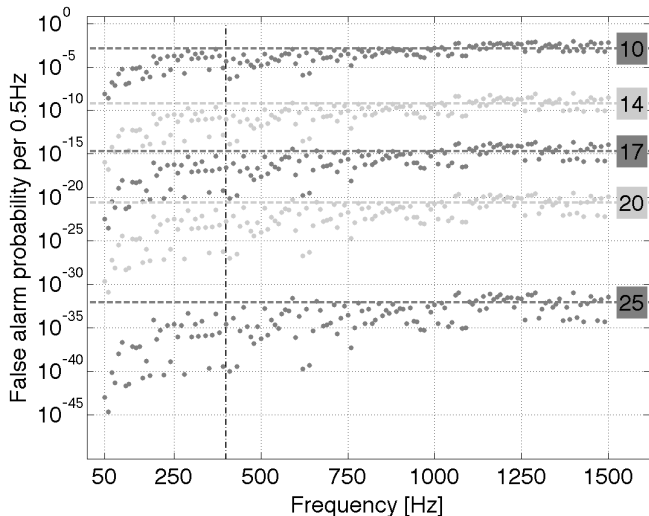


FIG. 3: False alarm probabilities $P_F(k; \mathcal{C}_{\max})$ as a function of frequency band (labeled by k) for different values of $\mathcal{C}_{\max} \in \{10, 14, 17, 20, 25\}$. The dashed horizontal lines represent the corresponding average across all frequencies. The vertical dashed line at 400 Hz indicates the separation between the low and high frequency ranges.

few candidates are expected to have 10 or more coincidences. Thus this will be the anticipated background level of coincidences, because from pure random noise one would not expect candidates of *more than* 10 coincidences in this analysis. In contrast, the false alarm probability of reaching the detection threshold of 20 or more coincidences per 0.5 Hz averaged over all frequency bands is about 10^{-21} . Therefore, this choice of detection threshold makes it extremely improbable to be exceeded in case of random noise.

V. ESTIMATED SENSITIVITY

The methods used here would be expected to yield very high confidence if a strong signal were present. To estimate the sensitivity of this detection scheme, Monte-Carlo methods are used to simulate a population of sources. The goal is to find the strain amplitude h_0 at which 10%, 50%, or 90% of sources uniformly populated over the sky and in their “nuisance parameters” would be confidently detected. In this analysis, “detectable” means “produces coincident events in 20 or more distinct data segments”. As discussed above, the false alarm probability for obtaining such a candidate in a given 0.5 Hz band is of order 10^{-21} . This is therefore an estimate of the signal strength required for high-confidence detection. For this purpose, the pipeline developed in [10] is run here, using the input data of the present analysis. A large number of distinct simulated sources (trials) are tested for detection. A “trial” denotes a single simulated source which is probed for detection. For a detailed description of the methodology, the reader is re-

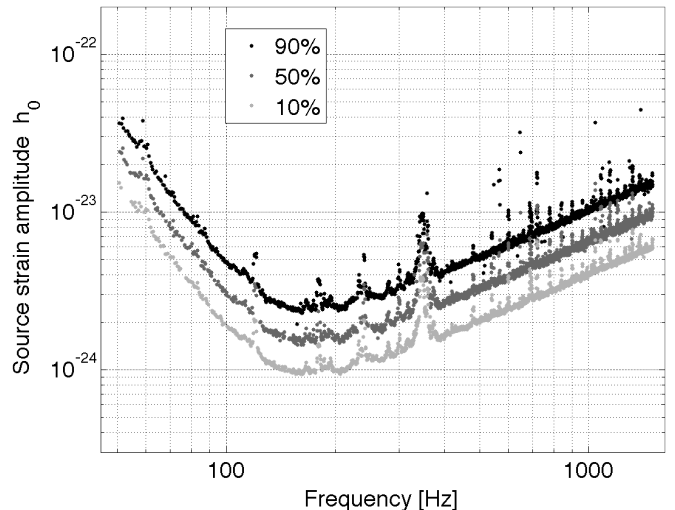


FIG. 4: Estimated sensitivity of the Einstein@Home search for isolated periodic GW sources in the early LIGO S5 data. The set of three curves shows the source strain amplitudes h_0 at which 10% (bottom), 50% (middle) and 90% (top) of simulated sources would be confidently detected in this Einstein@Home search.

ferred to [10].

Figure 4 shows the resulting search sensitivity curves as functions of frequency. Each data point on the plot denotes the results of 1000 independent trials. These show the values of h_0 as defined in [11] such that 10%, 50%, and 90% of simulated sources are confidently detected in the post-processing pipeline.

The dominant sources of error in these sensitivity curves are uncertainties in calibration of the LIGO detector response functions (cf. [10, 15]). The uncertainties range typically from about 8% to 15%, depending on frequency.

The behavior of the curves shown in Fig. 4 essentially reflects the instrument noise given in Fig. 1. One may fit the curves obtained in Fig. 4 to the shape of the harmonic-mean averaged strain noise power spectral density $S_h(f)$. Then the three sensitivity curves in Fig. 4 are described by

$$h_0^{\mathcal{D}}(f) \approx R_{\mathcal{D}} \sqrt{\frac{S_h(f)}{30 h}}, \quad (6)$$

where the pre-factors $R_{\mathcal{D}}$ for different detection probabilities levels $\mathcal{D} = 90\%$, 50% , and 10% are well fit below 400 Hz by $R_{90\%} = 29.4$, $R_{50\%} = 18.5$, and $R_{10\%} = 11.6$, and above 400 Hz by $R_{90\%} = 30.3$, $R_{50\%} = 19.0$, and $R_{10\%} = 11.8$.

VI. RESULTS

A. Vetoing instrumental noise lines

At the time the instrument data was prepared and cleaned, narrow-band instrumental line features of known origin were removed, as previously described in Sec. II. However, the data also contained stationary instrumental line features that were not understood, or were poorly understood, and thus were not removed *a priori*. After the search had been conducted, at the time the post-processing started, the origin of more stationary noise lines became known. Therefore, these lines, whose origin was tracked down after the search, are excluded (cleaned *a posteriori*) from the results. A list of the polluted frequency bands which have been cleaned *a posteriori* is shown in Tab. IV in the Appendix.

However, noise features still not understood instrumentally at this point were not removed from the results. As a consequence, the output from the post-processing pipeline contains instrumental artifacts that in some respects mimic periodic GW signals. But these artifacts tend to cluster in certain regions of parameter space, and in many cases they can be automatically identified and vetoed as done in previous searches [10, 23]. The method used here is derived in [24] and a detailed description of its application is found in [10].

For a coherent observation time baseline of 30 h the parameter-space regions where instrumental lines tend to appear are determined by global-correlation hypersurfaces [24] of the \mathcal{F} -statistic. On physical grounds, in these parameter-space regions there is little or no frequency Doppler modulation from the Earth's motion, which can lead to a relatively stationary detected frequency. Thus, the locations of instrumental-noise candidate events are described by

$$\left| \dot{f} + f \frac{\mathbf{v}_j}{c} \cdot \hat{\mathbf{n}} \right| < \epsilon, \quad (7)$$

where c denotes the speed of light, $\hat{\mathbf{n}}$ is a unit vector pointing to the source's sky-location in the SSB frame and relates to the equatorial coordinates α and δ by $\hat{\mathbf{n}} = (\cos \delta \cos \alpha, \cos \delta \sin \alpha, \sin \delta)$, \mathbf{v}_j is the orbital velocity of the Earth at the midpoint of the j 'th data segment ($|\mathbf{v}_j| \approx 10^{-4} c$). The parameter ϵ accounts for a certain tolerance needed due to the parameter-space gridding and can be understood as $\epsilon = \Delta f / N_c \Delta T$, where Δf denotes width in frequency (corresponding to the coincidence-cell width in the post-processing) up to which candidate events can be resolved during the characteristic length of time ΔT , and N_c represents the size of the vetoed or rejected region, measured in coincidence cells. In this analysis $\Delta T = 5\,718\,724\text{ s}$ (≈ 66 days) is the total time interval spanned by the input data.

Because false alarms are expected at the level of 10 coincidences, candidates that satisfy Eq. (7) for more than 10 data segments are eliminated (vetoed). The fraction of parameter space excluded by this veto is determined by

Monte-Carlo simulations to be about 13%. From Eq. (7) it follows that for fixed frequency the resulting fraction of sky excluded by the veto (uniformly averaged over spin-down) is greatest at lowest frequencies and decreases approximately as f^{-1} for higher frequencies. Appendix A of Ref. [10] presents an example calculation, illustrating the parameter-space volume excluded by this vetoing method.

B. Hardware-injected signals

During parts of the LIGO S5 run ten simulated periodic GW signals were injected at the hardware level, by modulating the interferometer mirror positions via signals sent to voice actuation coils surrounding magnets glued near the mirror edges. The hardware injections were active only part of the time during the S5 science run; in only 12 (of the 28) data segments chosen for this search did the hardware injections have duty cycles greater than 90%. But the value of 12 coincidences is far below the detection condition. Therefore, the hardware injections are not expected to be detected in this search, simply because they were inactive during a large fraction of the data analyzed.

C. Post-processing results

Figures 5 and 6 summarize all post-processing results from the entire search frequency range of 50 Hz to 1500 Hz, for each frequency coincidence cell maximized over the entire sky and full spin-down range.

In Fig. 5(a) all candidates that have 7 or more coincidences are shown in a sky projection. The color scale is used to indicate the number of coincidences. The most prominent feature still apparent forms an annulus of high coincidences in the sky, including the ecliptic poles, a distinctive fingerprint of the instrumental noise lines [24]. To obtain the results shown in Fig. 5(b), the set of candidates is cleaned *a posteriori* by removing strong instrumental noise lines, whose origin became understood after the search was begun, and excluding the hardware injections. Finally, in Fig. 5(c) the parameter-space veto is applied and coincidence cells which contain candidate events from a single detector only are excluded, too.

In Fig. 6(a) the coincidences and significance of all candidates that have 7 or more coincidences are shown as a function of frequency. From this set of candidates the hardware injections are excluded, strong instrumental noise lines of known origin are removed, the parameter-space veto is applied and finally single-detector candidates are excluded to obtain Fig. 6(b).

As can be seen from Figs. 5(c) and 6(b) there are no candidates that exceed the predefined detection threshold of 20 coincidences (which would initiate more an extensive investigation). The largest number of coincidences found is 10, which is at the background level of false

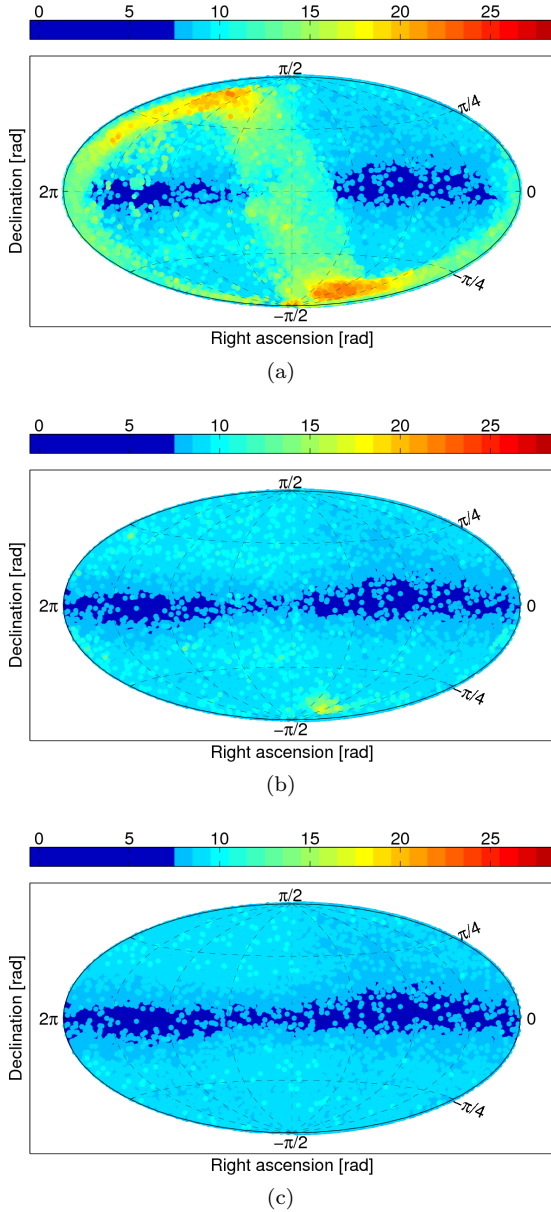


FIG. 5: Sky maps of post-processing results. Candidates having more than 7 coincidences are shown in Hammer-Aitoff projections of the sky. The color-bar indicates the number of coincidences of a particular candidate (cell). The top plot (a) shows the coincidence analysis results. In (b), *a posteriori* strong lines of known instrumental origin and hardware injections are removed. The bottom plot (c) is obtained by additionally applying the parameter-space veto and excluding single-detector candidates.

alarms expected from random noise only. From these candidates having 10 coincidences, Table II lists the ten most significant ones.

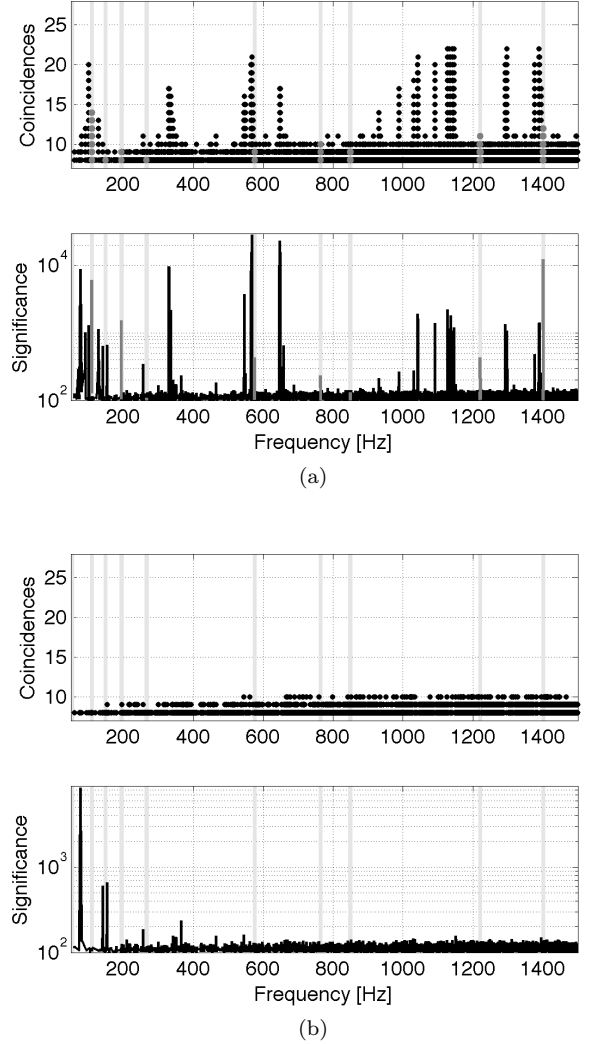


FIG. 6: The top plot (a) shows the post-processing candidates having more than 7 coincidences as function of frequency. The light-gray shaded rectangular regions highlight the frequency bands of the hardware injections. The dark-gray data points show the candidates resulting from the hardware-injected GW signals. In (b), the final results are shown after exclusion of instrumental lines of known origin and hardware injections, application of parameter-space veto and exclusion of single-detector candidates.

VII. COMPARISON WITH PREVIOUS SEARCHES

A previous paper [10] reported on the results of the Einstein@Home search for periodic GW signals in the LIGO S4 data. The present work extends this search analyzing more sensitive LIGO S5 data while using the same methods described in [10]. Therefore, this section elucidates the changes in configuration of the search and post-processing.

First, not only is more sensitive data used here, but a

TABLE II: The ten most significant post-processing candidates that have 10 or more coincidences. The frequency of each candidate f_{cand} refers to the fiducial GPS time $t_{\text{fiducial}} = 816\,397\,490$ s. The parameters δ_{cand} , α_{cand} , \dot{f}_{cand} , $\mathcal{C}_{\text{cand}} = \mathcal{C}_{\text{cand}}^{\text{H1}} + \mathcal{C}_{\text{cand}}^{\text{L1}}$ and $\mathcal{S}_{\text{cand}}$ are for the most-significant, most-coincident candidate with the given frequency of f_{cand} , where $\mathcal{C}_{\text{cand}}^{\text{H1}}$ and $\mathcal{C}_{\text{cand}}^{\text{L1}}$ denote the number of coincidences from detectors H1 and L1, respectively.

f_{cand} [Hz]	δ_{cand} [rad]	α_{cand} [rad]	\dot{f}_{cand} [Hz s ⁻¹]	$\mathcal{C}_{\text{cand}}$	$\mathcal{C}_{\text{cand}}^{\text{H1}}$	$\mathcal{C}_{\text{cand}}^{\text{L1}}$	$\mathcal{S}_{\text{cand}}$	P_{F} per 0.5Hz
543.810438	0.6823	5.9944	-3.24×10^{-10}	10	8	2	160.9	7.2×10^{-5}
1151.534608	1.1330	5.4462	2.11×10^{-11}	10	4	6	154.3	1.4×10^{-3}
1395.351068	-1.1928	2.5980	-3.92×10^{-9}	10	8	2	150.4	7.1×10^{-4}
1249.855062	-1.2380	6.0203	-2.43×10^{-9}	10	8	2	144.2	4.5×10^{-3}
1311.458030	-0.5143	6.1638	-3.32×10^{-9}	10	8	2	142.8	1.7×10^{-3}
1033.967720	0.6002	5.3133	-1.83×10^{-9}	10	8	2	142.7	1.2×10^{-3}
851.799376	1.1071	3.2019	-7.79×10^{-10}	10	8	2	142.1	4.1×10^{-4}
665.944644	-0.4602	2.3638	-1.28×10^{-9}	10	6	4	141.9	1.0×10^{-3}
669.187638	-0.6928	3.0333	-1.58×10^{-9}	10	7	3	141.6	1.0×10^{-3}
1443.831722	0.7046	6.0788	-4.47×10^{-9}	10	7	3	141.5	3.5×10^{-3}

larger total volume of data is searched compared to [10]. The number of 30-h data segments analyzed increased from 17 to 28.

In addition, the template grids used in each data segment of this search were constructed to be denser, reducing the possible loss of signals due to mismatch in the template waveforms. Compared to the previous search in S4 data, where a maximal mismatch of $m = 0.2$ ($m = 0.5$) was used in the low (high) frequency range, here templates are placed on a grid of higher density using $m = 0.15$ ($m = 0.4$) in the low (high) frequency range.

Moreover, in the high-frequency range a larger range of possible spin-downs is searched. The S4 analysis searched over minimum spin-down ages greater than 10 000 yr for frequencies in the higher range ($f > 300$ Hz), whereas this analysis searches over minimum spin-down ages greater than 8 000 yr for frequencies in the higher range ($f > 400$ Hz). The different partitioning of frequencies into the low and high ranges (split at 300 Hz in S4, split at 400 Hz here) is a consequence of an optimization study reflecting the overall most sensitive search at given computing power.

This search presented here analyzed in total about three times more workunits than in the S4 search. In searching the S4 data, each workunit returned the top 13 000 candidate events, whereas this search is designed to keep only the top 1 000 (10 000) candidate events in the low (high) frequency range. This configuration has the purpose of balancing the load on the Einstein@Home servers, which receive the workunit results. A low-frequency workunit returns a factor of 10 fewer events, because these were designed to last approximately 10 times less than each high-frequency workunit.

Finally, based on the estimates presented in Sec. V, the present search is overall about a factor of three more sensitive than the previous S4 search. This improvement is a consequence of using more sensitive detector data in combination with a finer-spaced template bank.

The methods used here, as well as in the S4 paper, would be expected to give very high confidence if a strong

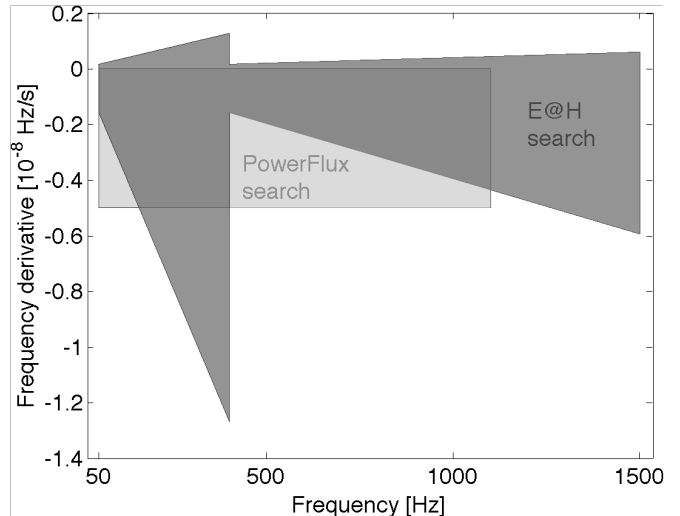


FIG. 7: Comparison of search parameter spaces in the plane of frequency and frequency derivative. The dark-gray region refers to this Einstein@Home all-sky analysis in early LIGO S5 data. The light-grey area corresponds to the recent all-sky PowerFlux search [15] in early LIGO S5 data.

enough signal were present in the data. It is interesting to compare the sensitivity of this detection scheme with the sensitivity of upper limits such as presented recently in [15]. Based on the PowerFlux method [23], that analysis set strain upper limits at the 95% confidence level in the frequency range of 50 – 1100 Hz and the frequency-derivative range of $-5 \times 10^{-9} - 0$ Hz s⁻¹ using 7 147 h of early LIGO S5 data, about 8.5 times more data than was used here. Note that this Einstein@Home search explores substantially larger parts of parameter space in frequency and frequency derivative, as shown in Fig. 7.

The upper-limit worst-case results of [15] for the equatorial sky region are remarkably close to the 90%-detection-level h_0 -values of Fig. 4. However, these PowerFlux upper limits refer to the most unfavorable polarization and sky position. A population-based upper limit over all sky locations and polarizations would be lower.

On the other hand, another key difference between the PowerFlux upper limits procedure and the sensitivity estimation carried out here is the detection criteria. In the present work, detection requires a signal to generate 20 or more coincidences among the 28 different data segments. This corresponds to a false alarm probability in Gaussian noise of the order 10^{-21} per 0.5 Hz frequency band. This is different from [15], where simulated signals are compared to the strongest candidates found. Thus, an equivalent detection criterion for this work would be to compare the signals against the strongest candidates in each 0.5 Hz band. These are typically 10 coincidences, which relates to a Gaussian noise false alarm rate of order 10^{-3} . One can estimate the effect on sensitivity by recomputing the sensitivity estimation of Sec. V, but requiring each signal to produce only 10 coincidences. This reduces the prefactors $R_{\mathcal{D}}$ given above by a factor of 1.24.

Apart from the larger parameter space searched, the present analysis is achieving roughly comparable sensitivity to [15] in spite of searching 8.5 times less data. Much of this effectiveness is due to the increased coherent integration time (30 hours vs 30 minutes), which is only possible due to the great amount of computing power donated by the tens of thousands of Einstein@Home volunteers.

VIII. CONCLUSION

Using early LIGO fifth-science-run data this paper reports on the results from the Einstein@Home search for unknown periodic GW sources, extending the previous Einstein@Home search in LIGO S4 data [10]. The sensitivity of the present analysis improves upon the previous Einstein@Home S4 search by a factor of about three. Additionally, in large regions of the parameter space probed, this analysis yields the currently most sensitive all-sky search results for periodic GW sources.

No credible periodic GW signal was found. Over a 100-Hz wide band around the detectors' most sensitive frequencies, more than 90% of sources with dimensionless gravitational-wave strain amplitude greater than 3×10^{-24} would have been detected.

While no statistically significant signal was observed in this analysis, the results demonstrate the capability of public distributed computing to accomplish a sensitive periodic GW search for the benefit of future searches.

The sensitivity of the present analysis is essentially limited by the first-stage threshold on \mathcal{F} -statistics forced by the limited data volume which can be returned from the participating clients. A new Einstein@Home search

currently underway carries out the incoherent combination of \mathcal{F} -statistic results on the client machines (done here in the post-processing once results were sent back). This makes it possible to set a much lower (sensitivity-optimized) first-stage threshold on \mathcal{F} -statistics. Hence, results from the new search promise a significant enhancement in the overall sensitivity for a periodic GW detection.

Acknowledgments

The authors thank the tens of thousands of volunteers who have supported the Einstein@Home project by donating their computer time and expertise for this analysis. Without their contributions, this work would not have been possible.

The authors gratefully acknowledge the support of the United States National Science Foundation for the construction and operation of the LIGO Laboratory and the Science and Technology Facilities Council of the United Kingdom, the Max-Planck-Society, and the State of Niedersachsen/Germany for support of the construction and operation of the GEO600 detector. The authors also gratefully acknowledge the support of the research by these agencies and by the Australian Research Council, the Council of Scientific and Industrial Research of India, the Istituto Nazionale di Fisica Nucleare of Italy, the Spanish Ministerio de Educación y Ciencia, the Conselleria d'Economia, Hisenda i Innovació of the Govern de les Illes Balears, the Royal Society, the Scottish Funding Council, the Scottish Universities Physics Alliance, The National Aeronautics and Space Administration, the Carnegie Trust, the Leverhulme Trust, the David and Lucile Packard Foundation, the Research Corporation, and the Alfred P. Sloan Foundation. This document has been assigned LIGO Laboratory document number LIGO-P0900032-v3.

APPENDIX A: CLEANED INSTRUMENTAL NOISE LINES

Table III lists the frequencies of noise lines excluded from the data and replaced by Gaussian noise *a priori* to the search. Table IV lists the central frequencies around either side of which the Doppler band ($\Delta f_{\text{Line}} = f_{\text{Line}} \times 10^{-4}$) is *a posteriori* excluded from the post-processed search results.

[1] A. Abramovici et al., *Science* **256**, 325 (1992).
 [2] B. C. Barish and R. Weiss, *Physics Today* **52**, 44 (1999).
 [3] L. Bildsten, *Ap. J.* **501**, L89 (1998).
 [4] B. J. Owen, L. Lindblom, C. Cutler, B. F. Schutz, A. Vec-

chio, and N. Andersson, *Phys. Rev. D* **58**, 084020 (1998).
 [5] G. Ushomirsky, C. Cutler, and L. Bildsten, *Mon. Not. Roy. Astron. Soc.* **319**, 902 (2000).
 [6] C. Cutler, *Phys. Rev. D* **66**, 084025 (2002).

TABLE III: Instrumental noise lines cleaned from H1 and L1 data. The three columns show the central frequency f_{Line} , the bandwidth $\Delta f_{\text{Line}}^{(1)}$ removed below the central frequency and the bandwidth $\Delta f_{\text{Line}}^{(2)}$ removed above the central frequency. Thus the total bandwidth removed per central frequency is $\Delta f_{\text{Line}}^{(1)} + \Delta f_{\text{Line}}^{(2)}$. In addition, at *each harmonic* of the 60 Hz mains frequency, the same bandwidth is also removed. A zero bandwidth indicates that the line-cleaning algorithm replaces in these cases a single Fourier bin with the average of bins on either side. The spacing between Fourier bins is 1/1800 Hz.

H1			L1		
$f_{\text{Line}}[\text{Hz}]$	$\Delta f_{\text{Line}}^{(1)}[\text{Hz}]$	$\Delta f_{\text{Line}}^{(2)}[\text{Hz}]$	$f_{\text{Line}}[\text{Hz}]$	$\Delta f_{\text{Line}}^{(1)}[\text{Hz}]$	$\Delta f_{\text{Line}}^{(2)}[\text{Hz}]$
46.7	0.0	0.0	54.7	0.0	0.0
60.0	1.0	1.0	60.0	1.0	1.0
346.0	4.0	4.0	345.0	5.0	5.0
393.1	0.0	0.0	396.7	0.0	0.0
686.9	0.3	0.3	686.5	1.0	1.0
688.2	0.3	0.3	688.83	0.5	0.5
689.5	0.5	0.6	693.7	0.7	0.7
694.75	1.25	1.25	1029.5	0.25	0.25
1030.55	0.1	0.1	1031	0.5	0.5
1032.18	0.04	0.04	1033.6	0.2	0.2
1032.58	0.1	0.1	1041	1.0	1.0
1033.7	0.1	0.1	1151.5	0.0	0.0
1033.855	0.05	0.05	1372.925	0.075	0.075
1034.6	0.4	0.4	1374.7	0.1	0.1
1041.23	0.1	0.1	1375.2	0.1	0.1
1042.0	0.5	0.2	1378.39	0.1	0.1
1043.4	0.2	0.2	1387.4	0.05	0.05
1144.3	0.0	0.0	1388.5	0.3	0.3
1373.75	0.1	0.1			
1374.44	0.1	0.1			
1377.14	0.1	0.1			
1378.75	0.1	0.1			
1379.52	0.1	0.1			
1389.06	0.06	0.06			
1389.82	0.07	0.07			
1391.5	0.2	0.2			

TABLE IV: Frequencies of instrumental lines that have been excluded *a posteriori* from the post-processed search results. Each column shows the central frequency f_{Line} around which a bandwidth of $\Delta f_{\text{Line}} = f_{\text{Line}} \times 10^{-4}$ has been removed on either side. The cleaned bandwidth corresponds to the maximum possible frequency shift due to the global parameter-space correlations [24]. On physical grounds this is related to the maximum possible Doppler shift due to the orbital velocity of the Earth, which is approximately 10^{-4} in units of the speed of light.

$f_{\text{Line}}[\text{Hz}]$	$f_{\text{Line}}[\text{Hz}]$	$f_{\text{Line}}[\text{Hz}]$	$f_{\text{Line}}[\text{Hz}]$
69.75	568.17	1030.55	1292.91
90.0	570.41	1042.19	1294.14
100.0	645.56	1043.33	1297.67
128.0	646.46	1092.01	1298.93
256.0	647.07	1128.28	1317.47
335.0	648.84	1132.22	1377.14
329.0	649.46	1136.23	1388.38
546.01	658.74	1142.87	1390.70
548.38	686.92	1145.29	1391.60
564.14	930.34	1146.59	
566.17	988.19	1291.11	

- [7] D. I. Jones and N. Andersson, Mon. Not. Roy. Astron. Soc. **331**, 203 (2002).
- [8] A. Melatos and D. J. B. Payne, Ap. J. **623**, 1044 (2005).
- [9] B. J. Owen, Phys. Rev. Lett. **95**, 211101 (2005).
- [10] B. Abbott et al. (The LIGO Scientific Collaboration), Phys. Rev. D **79**, 022001 (2009).
- [11] P. Jaranowski, A. Królak, and B. F. Schutz, Phys. Rev. D **58**, 063001 (1998).
- [12] P. Jaranowski and A. Królak, Phys. Rev. D **61**, 062001 (2000).
- [13] <http://einstein.phys.uwm.edu>.
- [14] B. Abbott et al. (The LIGO Scientific Collaboration), Phys. Rev. D **77**, 022001 (2008).
- [15] B. Abbott et al. (The LIGO Scientific Collaboration), Phys. Rev. Lett. **102**, 111102 (2009).
- [16] The Einstein@Home project is built upon the BOINC (Berkeley Open Infrastructure for Network Computing) architecture described at <http://boinc.berkeley.edu/>.
- [17] D. P. Anderson, in *GRID '04: Proceedings of the Fifth IEEE/ACM International Workshop on Grid Computing* (2004), pp. 4–10.
- [18] D. P. Anderson, C. Christensen, and B. Allen, in *SC '06: Proceedings of the 2006 ACM/IEEE conference on Supercomputing* (2006), p. 126.

-
- [19] R. Balasubramanian, B. S. Sathyaprakash, and S. V. Dhurandhar, Phys. Rev. D **53**, 3033 (1996).
- [20] B. J. Owen, Phys. Rev. D **53**, 6749 (1996).
- [21] B. Krishnan, B. J. Owen, R. Prix and A. M. Sintes, “Searching for isolated pulsars using Einstein@Home”, LIGO-T080340, 2008, available in <http://admbdbsrv.ligo.caltech.edu/dcc/>.
- [22] B. Abbott et al. (The LIGO Scientific Collaboration), Phys. Rev. D **76**, 082001 (2007).
- [23] B. Abbott et al. (The LIGO Scientific Collaboration), Phys. Rev. D **77**, 022001 (2008).
- [24] H. J. Pletsch, Phys. Rev. D **78**, 102005 (2008).